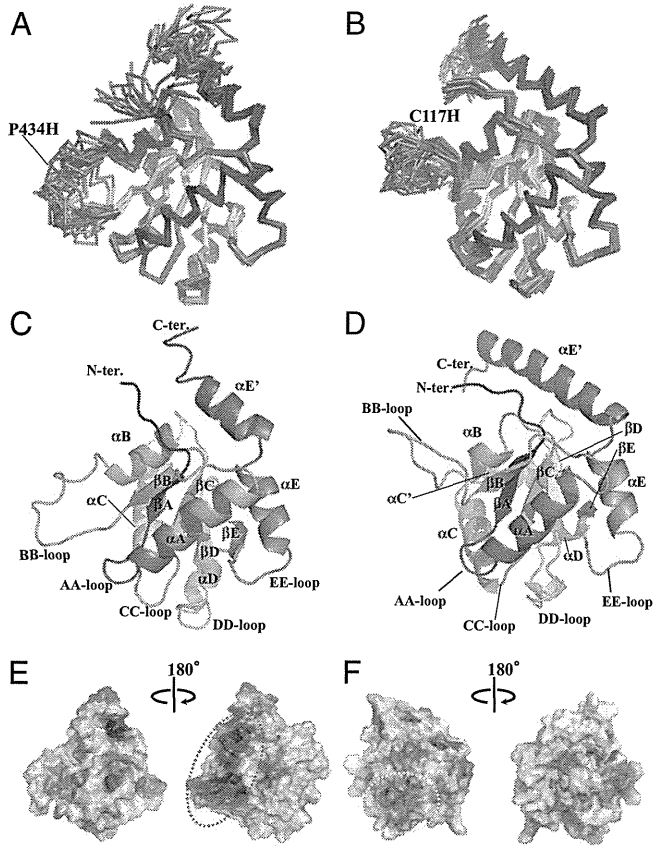

Fig. 2. Structures of the TICAM-1 and TICAM-2 TIR domains. (*A* and *B*) The overlay of the 20 lowest energy structures of the TIR domains of TICAM-1 and TICAM-2 determined by NMR. The backbone atoms (N, Cα, C′) of polypeptides are drawn in wire model; β-sheets in yellow; α-helices in red. Pro434 of TICAM-1 and Cys117 of TICAM-2 in BB-loop are substituted with His, which are shown in orange and labeled. (*C* and *D*) The TIR domain of TICAM-1 (*C*) and TICAM-2 (*D*) in ribbon model. β-strands, α-helices, and the connecting loops are labeled after the conventional nomenclature of the TIR domain (9). (*E* and *F*) Electrostatic surface potential of the TIR domains of TICAM-1 (*E*) and TICAM-2 (*F*). Positive, negative, and neutral electrostatic surface potentials are presented in blue, red, and white, respectively. The electrostatic surface potential in *E* and *F*, *Left* is presented as the same orientation as shown in *A* (*C*) and *B* (*D*). The opposite surfaces are shown in *E* and *F*, *Right*. The basic surface in TICAM-1 TIR and the acidic surface in TICAM-2 TIR are enclosed by red and yellow dotted lines, respectively.

Yeast two-hybrid analyses showed that TICAM-2 mutants bearing E87A/D88A/D89A and E197A/E198A could not grow completely on SD-LWHA medium due to disruption of their interaction with wild-type TICAM-1 (Fig. 3*C*), suggesting that the acidic cluster consisting of residues Glu87/Asp88/Asp89 in the AA-loop and Glu197/Glu198 in the EE-loop of the TICAM-2 TIR domain might be responsible for association with the TICAM-1 TIR domain (Fig. 3*D*, in magenta). However, in yeast two-hybrid experiments, it is generally difficult to distinguish mutations that disrupt the protein interaction surface from those that disrupt the tertiary structure. To discriminate these two scenarios, the mutant proteins were expressed and subjected to gel-filtration chromatography. We showed the results in *SI Text* and Fig. S3.

Coupled Mutations Identify Additional Binding Sites. Because dimer formation of the TICAM-2 TIR domain is indispensable for interaction with the TICAM-1 TIR domain, we used TICAM-2 TIR domain mutants that harbored no BB-loop mutations in the following yeast two-hybrid experiments. Because the β-strands formed a core structure surrounded by α-helices and loop regions, the residues in the β-strands would be expected to stabilize the structure of the TIR domain. Thus, we applied mutations to the exposed surface residues located on α-helices or loops, based on the NMR structure of TICAM-2 C117H (Fig. S4) and studied further interaction sites between the TICAM-2 and TICAM-1 TIR domains using yeast two-hybrid experiments. The heterotypic interaction between the TICAM-2 wild type and the TICAM-1 mutants was studied using an SD-LWH medium where the 3AT concentration is successively increased (Fig. 4*A*). Tables S2 and S3 list the results of the yeast two-hybrid experiments. Only TICAM-2 mutants involving residues on the CC′-loop between the αC and the αC′ helices showed reduced affinity for TICAM-1 as is summarized in Fig. 4*A*. First, the interaction of the F153A/Y154S, Y154S/T155A, and T155A/S156A mutants of the TICAM-2 TIR domain was studied with the wild type of the TICAM-2 TIR domain, showing that these mutants retain the homotypic interaction with the TICAM-2 wild type (Fig. 4*A*, right lane). Next, these mutants were applied to the yeast two-hybrid analyses to study heterotypic interactions with wild-type TICAM-1 and TICAM-1 P434H. Considering that monomeric TICAM-1 P434H can interact with the TICAM-2 dimer, the contact residues should be located near the RK site. Thus, we selected Gln518 and Ile519 on the EE-loop and αE-helix as further candidates for interaction with the TICAM-2 TIR domain.

Among the TICAM-2 TIR domain mutants F153A/Y154S, Y154S/T155A, and T155A/S156A, only the T155A/S156A mutant on the CC′-loop showed reduced interaction with wild type, P434H, and P434H/Q518A/I519A TICAM-1 mutants in a 3AT dose-dependent manner, with higher growth inhibition for the P434H/Q518A/I519A mutant. This result implied that Thr155 and Ser156 in TICAM-2 (designated the "TS site") and Gln518 and

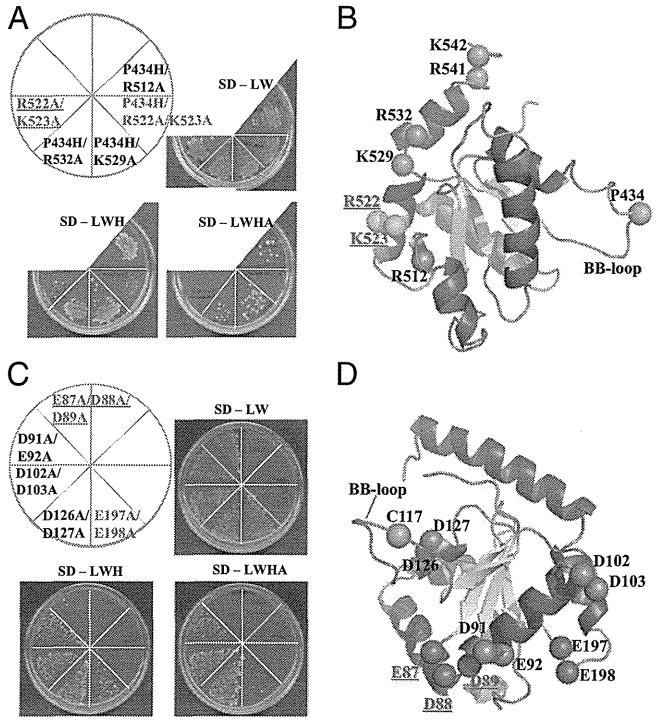

Fig. 3. Heterotypic interaction between TICAM-1 and TICAM-2 TIRs revealed by yeast two-hybrid assays (1). (*A*) Yeast two-hybrid assays using the wild type of the TICAM-2 TIR domain as bait and the mutants of the TICAM-1 TIR domain as prey. (*B*) The basic residues on the EE-loop and αE- and αE′-helices in the TICAM-1 TIR domain (shown as spheres) are mutated to Ala. The residues that disrupt the heterotypic interaction are displayed in cyan. The position of the BB-loop mutation in TICAM-1 TIR is shown in orange. (*C*) Yeast two-hybrid assays using the wild type of the TICAM-1 TIR domain as bait and the mutants of the TICAM-2 TIR domain harboring no BB-loop mutation as prey. (*D*) The acidic residues in the TICAM-2 TIR domain (shown as spheres) are mutated to Ala. The residues that disrupt the heterotypic interaction are displayed in magenta. The position of the BB-loop mutation in TICAM-2 TIR is shown in orange.

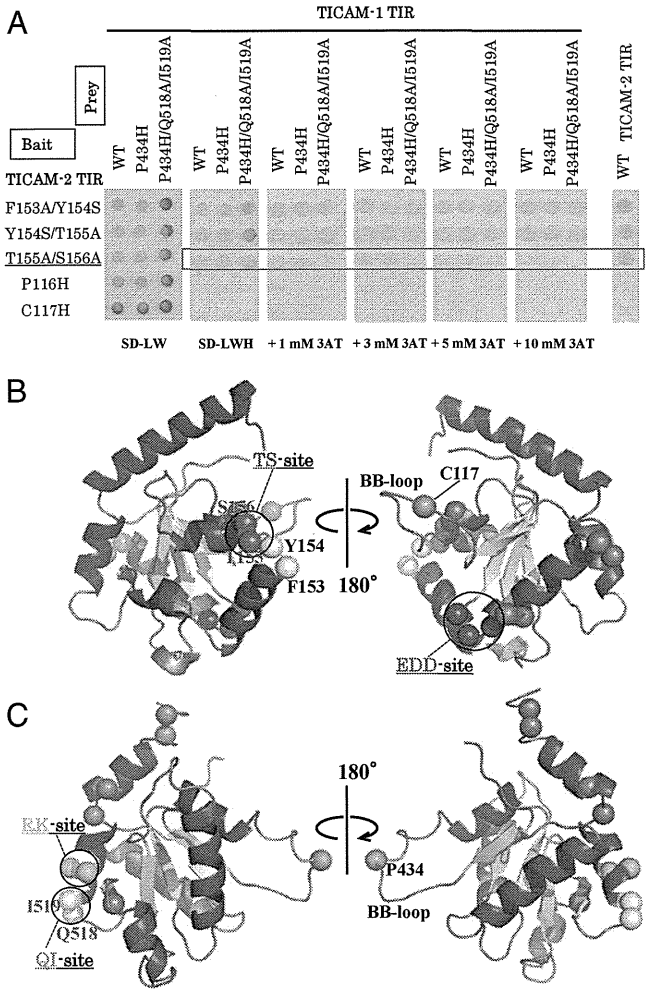

Fig. 4. Heterotypic interaction between TICAM-2 and TICAM-1 TIRs revealed by yeast two-hybrid assays (2). (*A*) Yeast two-hybrid assays using the mutants of TICAM-2 TIR as bait and the wild type and mutants of TICAM-1 TIR as prey. The wild-type TICAM-2 TIR is also used as prey as shown in *Right*. Yeast growth was analyzed with SD-LWH medium supplemented with 3-AT. (*B*) Residue mapping on the structure of TICAM-2 TIR. Thr155 and Ser156 are shown in blue (TS site), and Phe153 and Y154 are shown in white. Acidic residues, Glu87, Asp88, and Asp89 (EDD site), which are critical for interaction with TICAM-1, are shown in magenta. The residue C117 substituted by His is shown in orange. (*C*) Residue mapping on the structure of TICAM-1 TIR. Arg522 and Lys523 (RK site) are shown in cyan, and Gln518 and Ile519 (QI site) are shown in white. The Pro434 substituted by His in BB-loop of TICAM-1 is shown in orange.

Ile519 in TICAM-1 (designated the "QI site") are also involved in the heterotypic interaction (Fig. 4*A*). Intriguingly, the TS site in blue and the EDD site in magenta are located on opposite sides of the TICAM-2 TIR domain (Fig. 4*B*). In TICAM-1, the interacting residues with the TICAM-2 TIR domain are located on the RK site (in cyan) and QI site (in white), which form a wedge-like shape on the TICAM-1 TIR domain surface (Fig. 4*C*).

Restrained Docking of Trimeric TICAM-2/TICAM-1 Complex. The solution structures of the TICAM-1 P434H and TICAM-2 C117H mutants, along with the results of the mutagenesis and yeast two-hybrid assays, permitted docking of the complex formed by two TICAM-2 TIR domains and a single TICAM-1 TIR domain (*SI Text*, Fig. S5).

As shown in Fig. 5, the heterotypic interaction sites on TICAM-2 in the top-ranked model involve the acidic surface of the EDD site on the first TICAM-2 chain and the TS site on the second TICAM-2 chain, located on the opposite side (Fig. 5*A*). Significantly, the TICAM-2 homo-dimer positions the EDD and TS sites next to each other (Fig. 5*A*), forming a concave surface that can accommodate the TICAM-1 TIR domain. The interaction site on TICAM-1 includes the RK site on the αE-helix and the QI site on the EE-loop, which are located on the top of the wedge (Fig. 5*A*). In the top-scoring model, all 7 mutations that abrogated TICAM-2/TICAM-1 binding and 30 out of the 31 mutations that did not affect TICAM-2/TICAM-1 binding were recapitulated in the binding energy calculations (Table S4). The TICAM-2 dimer is symmetrically related by a twofold axis along the BB-loop and is maintained by the BB-loop and αC-helix interactions, respectively, consistent with the TLR10 dimer structure (Fig. 5*B*).

The top view of the interaction surface between the TICAM-2 dimer and the TICAM-1 monomer is shown in Fig. 5*C*, where the binding surface of TICAM-2 is represented by the electrostatic surface potential and TICAM-1 by a ribbon model. As shown in the figure, the RK site interacts with the acidic surface of the EDD site, and the QI site with the TS site (Fig. 5*C*).

Reporter Gene and Binding Assays Using Full-Length TICAM-1 and TICAM-2 Mutants. Based on the yeast two-hybrid analysis, we constructed mammalian expression vectors coding the wild type and various mutants of TICAM-2 and TICAM-1 and measured their IFN-β promoter activation abilities by reporter gene assays. Forcedly expressed wild type TICAM-2 activated the IFN-β promoter in HEK293FT cells in a dose-dependent manner (Fig. 6*A*). In contrast, the TICAM-2 EDD-site mutant E87A/D88A/D89A failed to activate the IFN-β promoter (Fig. 6*A*). Overexpressed TICAM-2 undergoes homo-dimerization, which in turn recruits TICAM-1, resulting in activation of the IFN-β promoter. Therefore, we next analyzed TICAM-2–TICAM-1-dependent IFN-β promoter activation in the presence of limiting amounts of TICAM-1. A marked enhancement of TICAM-1-mediated IFN-β promoter activation was observed with wild-type TICAM-2, and to a lesser extent with the EDD-site TICAM-2 mutant (Fig. 6*B*). In the case of TICAM-1, the RK-site mutant (R522A/K523A) only weakly activated the IFN-β promoter (Fig. 6*C*), consistent with the predicted electrostatic interaction between the acidic surface of the TICAM-2 TIR domain and the basic surface of TICAM-1 observed in the yeast two-hybrid experiments and the docking model. We also measured the NF-κB activation abilities of the EDD-site mutant of TICAM-2 (Fig. S6). Both IFN-β and NF-κB promoter assays demonstrated that the TICAM-2 EDD-site mutant suppressed both signals.

To confirm that the TICAM-2 EDD site is involved in the binding of TICAM-1 TIR domain, a coimmunoprecipitation assay was performed in HEK293FT cells. Although the expression level of TICAM-1, the TICAM-2 wild type, and the TICAM-2 EDD mutant in HEK293FT cells was similar (Fig. S7, *Lower*), the affinity between the TICAM-2 mutant and TICAM-1 was much reduced compared with that between the TICAM-2 wild type and TICAM-1 (Fig. S7, *Upper*). All of the data suggest that the reduced IFN-β promoter activity of the TICAM-2 EDD mutant was due to its reduced affinity to TICAM-1.

Discussion

The oligomerization properties of TIR domains are closely related to their biological functions. This study presents challenges for structural analysis by NMR. Here, we applied dominant-negative BB-loop mutations to the TICAM-1 and TICAM-2 TIR domains that disrupted the oligomerization. To study the interaction between TICAM-1 and TICAM-2 TIR domains, we used yeast two-hybrid experiments in combination with monomeric structural information. Although the yeast two-hybrid method can produce false positives, we could eliminate such false positives by structural analysis of the BB-loop mutants together with gel-filtration studies of the expressed proteins. Using this approach, we identified two binding regions, the EDD site and the TS site, located on the opposite sides of TICAM-2. Our docking calculations, based on yeast two-hybrid data, revealed a TICAM-2 TIR homo-dimer that assumed a twofold axis of

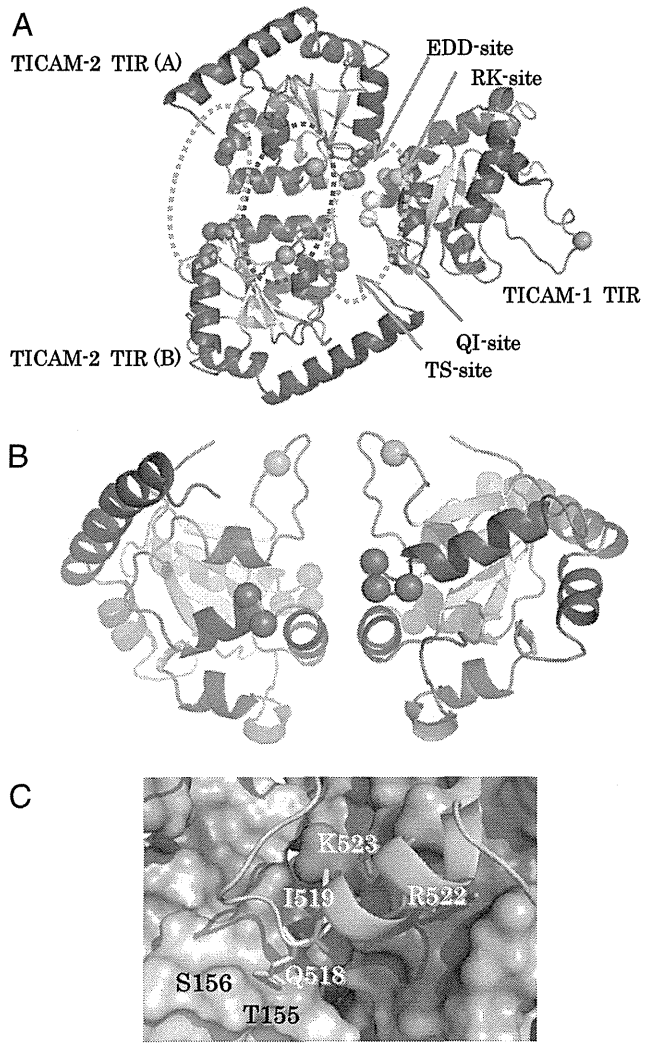

Fig. 5. Docking model of the TIR domains of TICAM-2 and TICAM-1. (*A*) The docking structure comprised of TICAM-2 dimer and TICAM-1 monomer. Homotypic and heterotypic interfaces are enclosed by blue and orange dotted lines, respectively. (*B*) TICAM-2 dimer presenting the binding surface with TICAM-1 TIR. The EDD and TS sites are located at the front surface (also at the back surface) that interact with the wedge of the TICAM-1 TIR (the RK and QI sites). (*C*) The front view of the interacting surface of TICAM-2 is shown in electrostatic surface potential presentation whereas the wedge of the TICAM-1 is presented in ribbon model. The residues on the RK and QI sites are shown in wire model and labeled.

symmetry around the BB-loop, similar to the TLR10 TIR domain structure. Importantly, the two binding regions revealed by the yeast two-hybrid experiments are spatially close in this TICAM-2 homo-dimer structure (Fig. 5*A*). Heterotypic interaction sites on the TICAM-1 TIR domain could also be elucidated by our approach, which indicated that the RK and QI sites are responsible for interaction with TICAM-2. It is notable that this heterotypic interaction does not require dimer formation of the TICAM-1 TIR domain. In our restraint-driven docked model, the wedge-shaped surface containing the RK and QI sites binds to the concave surface formed by the EDD and TS sites belonging to different TICAM-2 TIR domains (Fig. 5 *A* and *B*).

An important conclusion derived from the present study is that the homo-dimerization of the TICAM-2 TIR domains presents a surface that recruits the monomeric moiety of the TICAM-1 TIR domain. In our previous reports, we showed that TLR4 binds the TICAM-2 wild type, but the interaction is disrupted by the BB-loop mutation of TLR4, whereas the BB-loop mutant of TICAM-2 still binds to TLR4 wild type based on the yeast two-hybrid experiments (1). We also showed that the TICAM-1 BB-loop mutant still interacts with the TIR domain of TLR3 wild type (27). Taken together, these results suggest a unique paradigm in which dimer formation of the upstream TIR domain is essential for recruitment of the monomeric moiety of the downstream TIR dimer. Consistent with this paradigm, BB-loop mutants of TLR3 and TLR4 as well as TICAM-1 and TICAM-2 completely abrogate downstream signaling.

It is notable that the myristoylation of TICAM-2 at the N terminus is essential for its localization on the plasma membrane or endosome, and colocalization with TLR4 (32). Interestingly, according to the present TICAM-2 TIR dimer model, the N termini of both TICAM-2 TIR domains are oriented in the same direction, permitting anchoring of the TICAM-2 dimer to the membrane.

A current consensus is that LPS on the surface of Gram-negative bacteria induces clustering of TLR4, leading to formation of the active TLR4 TIR dimer, which triggers activation of the MyD88 and TICAM-1 pathways. Recently, the structure of the Myddosome, a molecular complex mediated by the death domains of MyD88, IRAK4, and IRAK1/2, was determined (33–35). This TICAM-1/2 structural study, on the other hand, would allow us to speculate a model that the TLR4 TIR dimer bridges the TICAM-2 TIR dimer, which further couples with the TICAM-1 TIR, generating an extended signaling network downstream of TLR4. The present work proposes a key for future analysis about an IFN-inducing signaling complex in the context of TLR4-mediated LPS signaling. Recent studies showed the importance of lateral TLR3 clustering mediated by TICAM-1 for downstream signaling (36), consistent with our model.

Our reconstitution study revealed that the TICAM1/2 heterodimer formation is reproducible in HEK293FT cells and that TICAM-2 EDD mutant has less ability to recruit TICAM-1 than wild type (Fig. S7). Reporter activity reflecting IFN induction is accordingly decreased (Fig. 6). Thus, the proposed model is at least right in the formation of the two-adaptor complex. However, herein we only abstracted the complex of TICAM-1 and TICAM-2 from the IFN-inducing axis of LPS signaling of TLR4, which consists of an array of many different molecules. Reconstituting the optimal LPS–IFN signal axis in human TICAM-2 knockout cells will be required to test physiological importance of the TICAM-2 EDD domain.

Materials and Methods

For details, see *SI Materials and Methods*.

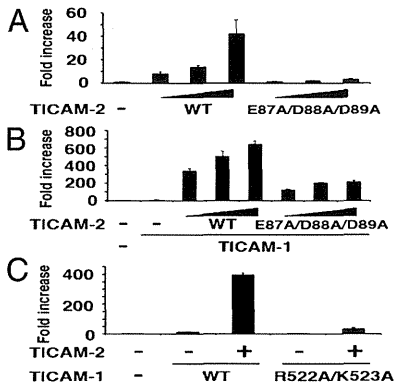

Fig. 6. Functional assays of TICAM-1 and TICAM-2 mutants in mammalian cells. (*A*) TICAM-2–dependent IFN-β promoter activation. IFN-β promoter activity was reduced by the E87A/D88A/D89A mutation in TICAM-2. (*B*) TICAM-2-TICAM-1–dependent IFN-β promoter activation. IFN-β promoter activity was reduced by the E87A/D88A/D89A mutation in TICAM-2. (*C*) TICAM-2-TICAM-1–dependent IFN-β promoter activation. The mutation of R522/K523 in TICAM-1 reduced IFN-β promoter activation.

Protein Expression and Purification. The human TICAM-1 gene encoding the TIR domain (387–545) with mutation of Pro434 to His was cloned into the pET22b (Novagen) vector. The human TICAM-2 gene encoding the TIR domain (75–235) with mutation of Cys117 to His was cloned into the pGEX6p-1 (GE healthcare) vector.

NMR Measurements and Structure Calculation. NMR data for chemical shift assignments for TICAM-1 P434H and TICAM-2 C117H were collected using a suite of triple resonance experiments on Varian UNITY INOVA 600 and 800 spectrometers.

Yeast Two-Hybrid Analysis. The TIR domains were constructed by direct cloning of two-step PCR products using mutant oligonucleotide primers and subcloned into pGBKT7 and pGADT7 plasmid (Clontech).

Restrained Docking Calculations. Two docking calculations were made to generate representative TICAM-2 TIR homo-dimer models, from which trimeric TICAM-2/TICAM-1 models were then constructed.

Luciferase Reporter Gene Assay. Mutants of TICAM-1(1–566) and TICAM-2(1–235) were generated using PCR and subcloned into pEF-BOS vector.

Immunoprecipitation and Immunoblot Analysis. FLAG-tagged TICAM-2 were immunoprecipitated using anti-FLAG mAb (2.5 μg per sample) and Protein G Sepharose (GE healthcare).

ACKNOWLEDGMENTS. This research is supported by the Japan Society for the Promotion of Science through its "Funding Program for World-Leading Innovative R&D on Science and Technology."

1. Oshiumi H, et al. (2003) TIR-containing adapter molecule (TICAM)-2, a bridging adapter recruiting to toll-like receptor 4 TICAM-1 that induces interferon-beta. *J Biol Chem* 278(50):49751–49762.
2. Oshiumi H, Matsumoto M, Funami K, Akazawa T, Seya T (2003) TICAM-1, an adaptor molecule that participates in Toll-like receptor 3-mediated interferon-beta induction. *Nat Immunol* 4(2):161–167.
3. Yamamoto M, et al. (2003) TRAM is specifically involved in the Toll-like receptor 4-mediated MyD88-independent signaling pathway. *Nat Immunol* 4(11):1144–1150.
4. Takeuchi O, Akira S (2010) Pattern recognition receptors and inflammation. *Cell* 140(6):805–820.
5. Yamamoto M, Takeda K, Akira S (2004) TIR domain-containing adaptors define the specificity of TLR signaling. *Mol Immunol* 40(12):861–868.
6. Gay NJ, Gangloff M, Weber AN (2006) Toll-like receptors as molecular switches. *Nat Rev Immunol* 6(9):693–698.
7. Gay NJ, Gangloff M (2007) Structure and function of Toll receptors and their ligands. *Annu Rev Biochem* 76:141–165.
8. Fitzgerald KA, et al. (2003) LPS-TLR4 signaling to IRF-3/7 and NF-kappaB involves the toll adapters TRAM and TRIF. *J Exp Med* 198(7):1043–1055.
9. Xu Y, et al. (2000) Structural basis for signal transduction by the Toll/interleukin-1 receptor domains. *Nature* 408(6808):111–115.
10. Tao X, Xu Y, Zheng Y, Beg AA, Tong L (2002) An extensively associated dimer in the structure of the C713S mutant of the TIR domain of human TLR2. *Biochem Biophys Res Commun* 299(2):216–221.
11. Khan JA, Brint EK, O'Neill LA, Tong L (2004) Crystal structure of the Toll/interleukin-1 receptor domain of human IL-1RAPL. *J Biol Chem* 279(30):31664–31670.
12. Ohnishi H, et al. (2009) Structural basis for the multiple interactions of the MyD88 TIR domain in TLR4 signaling. *Proc Natl Acad Sci USA* 106(25):10260–10265.
13. Valkov E, et al. (2011) Crystal structure of Toll-like receptor adaptor MAL/TIRAP reveals the molecular basis for signal transduction and disease protection. *Proc Natl Acad Sci USA* 108(36):14879–14884.
14. Lin Z, Lu J, Zhou W, Shen Y (2012) Structural insights into TIR domain specificity of the bridging adaptor Mal in TLR4 signaling. *PLoS ONE* 7(4):e34202.
15. Chan SL, Mukasa T, Santelli E, Low LY, Pascual J (2010) The crystal structure of a TIR domain from Arabidopsis thaliana reveals a conserved helical region unique to plants. *Protein Sci* 19(1):155–161.
16. Bernoux M, et al. (2011) Structural and functional analysis of a plant resistance protein TIR domain reveals interfaces for self-association, signaling, and autoregulation. *Cell Host Microbe* 9(3):200–211.
17. Chan SL, et al. (2009) Molecular mimicry in innate immunity: Crystal structure of a bacterial TIR domain. *J Biol Chem* 284(32):21386–21392.
18. Nyman T, et al. (2008) The crystal structure of the human toll-like receptor 10 cytoplasmic domain reveals a putative signaling dimer. *J Biol Chem* 283(18):11861–11865.
19. Poltorak A, et al. (1998) Defective LPS signaling in C3H/HeJ and C57BL/10ScCr mice: Mutations in Tlr4 gene. *Science* 282(5396):2085–2088.
20. Gautam JK, Ashish, Comeau LD, Krueger JK, Smith MF, Jr. (2006) Structural and functional evidence for the role of the TLR2 DD loop in TLR1/TLR2 heterodimerization and signaling. *J Biol Chem* 281(40):30132–30142.
21. Dunne A, Ejdeback M, Ludidi PL, O'Neill LA, Gay NJ (2003) Structural complementarity of Toll/interleukin-1 receptor domains in Toll-like receptors and the adaptors Mal and MyD88. *J Biol Chem* 278(42):41443–41451.
22. Li C, Zienkiewicz J, Hawiger J (2005) Interactive sites in the MyD88 Toll/interleukin (IL) 1 receptor domain responsible for coupling to the IL1β signaling pathway. *J Biol Chem* 280(28):26152–26159.
23. Radons J, et al. (2003) The interleukin 1 (IL-1) receptor accessory protein Toll/IL-1 receptor domain: analysis of putative interaction sites in vitro mutagenesis and molecular modeling. *J Biol Chem* 278(49):49145–49153.
24. Bovijn C, et al. (2012) Identification of interaction sites for dimerization and adapter recruitment in Toll/interleukin-1 receptor (TIR) domain of Toll-like receptor 4. *J Biol Chem* 287(6):4088–4098.
25. Núñez Miguel R, et al. (2007) A dimer of the Toll-like receptor 4 cytoplasmic domain provides a specific scaffold for the recruitment of signalling adaptor proteins. *PLoS ONE* 2(8):e788.
26. Seya T, Oshiumi H, Sasai M, Akazawa T, Matsumoto M (2005) TICAM-1 and TICAM-2: Toll-like receptor adapters that participate in induction of type 1 interferons. *Int J Biochem Cell Biol* 37(3):524–529.
27. Funami K, Sasai M, Oshiumi H, Seya T, Matsumoto M (2008) Homo-oligomerization is essential for Toll/interleukin-1 receptor domain-containing adaptor molecule-1-mediated NF-kappaB and interferon regulatory factor-3 activation. *J Biol Chem* 283(26):18283–18291.
28. Holm L, Park J (2000) DaliLite workbench for protein structure comparison. *Bioinformatics* 16(6):566–567.
29. Kawabata T (2003) MATRAS: A program for protein 3D structure comparison. *Nucleic Acids Res* 31(13):3367–3369.
30. Kawabata T, Nishikawa K (2000) Protein structure comparison using the markov transition model of evolution. *Proteins* 41(1):108–122.
31. Chien CT, Bartel PL, Sternglanz R, Fields S (1991) The two-hybrid system: A method to identify and clone genes for proteins that interact with a protein of interest. *Proc Natl Acad Sci USA* 88(21):9578–9582.
32. Rowe DC, et al. (2006) The myristoylation of TRIF-related adaptor molecule is essential for Toll-like receptor 4 signal transduction. *Proc Natl Acad Sci USA* 103(16):6299–6304.
33. Lin SC, Lo YC, Wu H (2010) Helical assembly in the MyD88-IRAK4-IRAK2 complex in TLR/IL-1R signalling. *Nature* 465(7300):885–890.
34. Gay NJ, Gangloff M, O'Neill LA (2011) What the Myddosome structure tells us about the initiation of innate immunity. *Trends Immunol* 32(3):104–109.
35. Kersse K, Verspurten J, Vanden Berghe T, Vandenabeele P (2011) The death-fold superfamily of homotypic interaction motifs. *Trends Biochem Sci* 36(10):541–552.
36. Luo J, et al. (2012) Lateral clustering of TLR3:dsRNA signaling units revealed by TLR3ecd:3Fabs quaternary structure. *J Mol Biol* 421(1):112–124.

Supporting Information

Enokizono et al. 10.1073/pnas.1222811110

SI Text

Comparison of NMR Spectra of Wild Type and BB-Loop Mutant. To exclude the possibility that the BB-loop mutations disrupt the tertiary structure of the TIR domain, we compared [^{1}H, ^{15}N]-HSQC spectra of both wild-type and TICAM-2 C117H under dilute solution conditions. At 50 μM concentration, the [^{1}H, ^{15}N]-HSQC spectra of the wild type and TICAM-2 C117H (Fig. S1 *A* and *B*) were quite similar, showing that TICAM-2 C117H has a similar structure to the wild type although the signal intensity of the wild type was significantly reduced as a result of oligomerization. The crystal structures of the TIR domains of the wild type and the BB-loop mutant of TLR2 are nearly identical (1), supporting a general model in which the BB-loop mutations do not disrupt the global TIR domain fold. Despite global reduction of the signal intensities in the wild type compared with TICAM-2 C117H, BB-loop residues showed remarkably reduced signal intensity, suggesting that the BB-loop residues are broadened due to dynamic equilibrium between the monomeric and oligomeric states. The exchange broadening effect on Leu122 in the wild type of TICAM-2 TIR and TICAM-2 C117H (Fig. S1 *A* and *B*) was significantly different, consistent with a model in which the homotypic interaction is directly mediated by the BB-loop residues. Although we could not observe NMR spectra of the wild-type TICAM-1 TIR even at dilute concentration, the solubility of TICAM-1 P434H was much improved, and we could obtain a clear NMR spectrum (Fig. S1*C*). After further optimization of the solution condition of the BB-loop mutants, the solubility of TICAM-2 C117H and TICAM-1 P434H was further improved, and the structures of the TIR domains were determined by NMR.

Confirmation of the Yeast Two-Hybrid Experiments by Gel-Filtration Chromatography. In yeast two-hybrid experiments, it is generally difficult to distinguish mutations that disrupt the protein interaction surface from those that disrupt the tertiary structure. To discriminate these two scenarios, the mutant proteins were expressed and subjected to gel-filtration chromatography. Both TICAM-2 C117H and TICAM-2 C117H/E87A/D88A/D89A appeared in the monomer position (Fig. S3 *A* and *B*), but TICAM-2 C117H/E197R/E198R appeared in the void, possibly due to disruption of the tertiary structure (Fig. S3*C*). The NMR structure of TICAM-2 C117H suggests that Glu197 and Glu198 form a salt bridge with Arg95, which raised the possibility that the mutation of Glu197 and Glu198 might destabilize the tertiary structure of the TICAM-2 TIR domain. Therefore, TICAM-2 C117H/R95E was prepared and subjected to gel-filtration chromatography. TICAM-2 C117H/R95E appeared in the void (Fig. S3*D*). Taken together, these results suggest that residues, E87, D88, and D89 of TICAM-2 C117H (designated the "EDD site") interact with Arg522 and Lys523 (the "RK site") on TICAM-1. Gel-filtration chromatography also resulted in TICAM-1 P434H appearing in the monomer position (Fig. S3*E*), consistent with the NMR result (Fig. S1*C*). However, the TICAM-1 P434H/E493R mutant appeared in the void, suggesting that the E493R mutation disrupts the tertiary structure of TICAM-1.

Restrained Docking of Trimeric TICAM-2/TICAM-1 Complex. An optimal model could be identified by considering mutational effects on binding in detail. That is, for each candidate trimer model, a series of mutations were generated *in silico* along with the corresponding changes in binding energy (Table S4). These changes were compared with the yeast two-hybrid assays for each mutant (Tables S2 and S3), and the candidate trimer models were ranked by their agreement with experiment. From such analysis, a narrow cluster consisting of five models (ranks 1, 2, 3, 7, and 8) was defined (Fig. S5).

Reporter Gene Assays of TICAM-1 and TICAM-2 Mutants in Mammalian Cells. TICAM-2-dependent IFN-β promoter activation was studied by the mutation of E87A/D88A/D89A. HEK293FT cells preseeded onto 96-well plates were transfected with empty vector or increasing amounts of expression vector for wild type or mutant TICAM-2 (10, 20, 70 ng per well) together with IFN-β promoter plasmid (25 ng per well) and internal control plasmid (5 ng per well). The total amount of DNA was kept at 100 ng per well by adding empty plasmid. Luciferase activity was measured 24 h after transfection. Next, TICAM-2-TICAM-1–dependent IFN-β promoter activation was studied by the mutation of E87A/D88A/D89A in the similar condition mentioned above with a limiting amount of TICAM-1 expression plasmid (0.1 ng per well). Finally, TICAM-2-TICAM-1–dependent IFN-β promoter activation was studied by the mutation of R522A/K523A in TICAM-1. Cells were transfected with empty vector or expression vector for wild type or mutant TICAM-1 (1 ng per well) and wild-type TICAM-2 (20 ng per well).

All experiments were done in triplicate, and data are shown as means ± SD. Representative data from a minimum of three separate experiments are shown.

Coimmunoprecipitation Assay of TICAM2 and TICAM2 EDD Mutant with TICAM-1. HEK293FT cells preseeded onto six-well plates were transfected with TICAM-1 expression vector (0.2 μg per well), TLR4 and MD2 expression vector (0.2 μg per well), and TICAM-2 expression vector (0.3 μg per well). The total amount of DNA was kept at 2 μg per well by adding empty plasmid. After 24 h from transfection, cells were harvested, and immunoprecipitation assays were performed.

SI Materials and Methods

Protein Expression and Purification. The human TICAM-1 gene encoding the TIR domain (amino acid residues 387–545) with mutation of Pro434 to His was cloned into the pET22b (Novagen) vector with restriction enzymes, NdeI and XhoI (GenBank accession no. NM_182919) and expressed as a His_6-tagged fusion protein at the N terminus. The human TICAM-2 gene encoding the TIR domain (amino acid residues 75–235) with mutation of Cys117 to His was cloned into the pGEX6p-1(GE healthcare) vector with restriction enzymes BamHI and EcoRI (GenBank accession no. NM_021649) and expressed as a GST fusion protein at the N terminus. These vectors were transformed into *Escherichia coli* BL21(DE3) that contains the chaperone expression plasmid pG-Tf2 (Takara). The transformed *E. coli* BL21(DE3) cells were cultured at 37 °C until the OD_{600} reached ~0.6–0.7. The cells were induced with 0.5 mM IPTG and 5 ng/mL tetracycline and then cultured for 18–20 h at 22 °C. The cells were resuspended in lysis buffer [20 mM Tris·HCl (pH7.0), 5 mM DTT, 5 mM EDTA, protease inhibitor mixture (Nacalai) except salts]. TICAM-1 P434H fused with His_6-tag was first purified by Ni^{2+}-NTA affinity chromatography. In contrast, TICAM-2 C117H was purified by Glutathione Sepharose 4B FF affinity chromatography, followed by PreScission protease cleavage. TICAM-1 P434H and TICAM-2 C117H were further purified by size-exclusion chromatography (HiLoad26/60 Superdex-75 pg column; GE Healthcare) in 50 mM Hepes (pH7.0), 10 mM DTT, 75 mM NaCl, and 0.1 mM EDTA.

The pooled fractions of each domain were applied to dialysis and buffer exchange with long-term stabilizing buffer [20 mM AcOH-AcONa (pH 5.0), 10 mM DTT, and 0.1 mM EDTA for TICAM-1 P434H and 40 mM Hepes-NaOH (pH 7.4), 10 mM DTT, 0.1 mM EDTA, and 5% (vol/vol) glycerol for TICAM-2 C117H, respectively].

Finally, each sample solution was concentrated with centricon-3 (MWCO 3 kDa) and exchanged in NMR buffer. NMR Samples were prepared at 0.5 mM TICAM-1 P434H, 20 mM AcOH-AcONa (pH 5.0), 5 mM DTT, 0.1 mM EDTA, 10% D_2O/H_2O, and 0.5 mM TICAM-2 C117H, 40 mM Hepes –NaOH (pH 7.4), 5 mM DTT, 0.1 mM EDTA, 5%(vol/vol) d_{11}-glycerol, 10% D_2O/ 90% H_2O.

NMR Measurements and Structure Calculation. NMR data for chemical shift assignments for TICAM-1 P434H and TICAM-2 C117H were collected using the suite of triple resonance experiments on Varian UNITY INOVA 600 and 800 spectrometers equipped with a cryogenically cooled probe at 298 K and 293 K, respectively. The data were processed with the NMRPipe software (2) and analyzed using the Sparky3 program (version 3.114) (3). NOE distance restraints were obtained from 3D ^{15}N-NOESY-HSQC (100 ms mixing time) and ^{13}C-NOESY-HSQC spectra (100 ms mixing time). The NMR structures of TICAM-1 P434H and TICAM-2 C117H were determined using the CANDID/CYANA 2.1 (4). Dihedral restraints were derived from backbone chemical shifts using TALOS (5). Chemical shift assignments and NOE and dihedral restraint data have been deposited at BMRB (accession nos. 18882 and 18883 for TICAM-2 and TICAM1, respectively), and the coordinates for the ensemble have been deposited in the Protein Data Bank (PDB ID codes 2mlw and 2mlx for TICAM-2 and TICAM1, respectively).

Yeast Two-Hybrid Analysis. The TIR domains were constructed by direct cloning of two-step PCR products using mutant oligonucleotide primers (6) and subcloned into pGBKT7 and pGADT7 plasmid (Clontech). All mutants were sequenced to confirm the mutation. Yeast two-hybrid assays were conducted in yeast diploid strain, mated with AH109 and Y187, in MATCHMAKER Two-Hybrid System 3 (Clontech).

Liquid cultures were incubated overnight with shaking (220 rpm) at 28 °C and normalized for cell concentration by dilution with synthetic dropout medium (SD medium) such that A_{600nm} = 0.1. After dilution serially, yeast cells were streaked or spotted onto appropriate selection plates and incubated at 28 °C for ~72 h. Interactions between TIR domains of TICAM-1 P434H and TICAM-2 C117H were screened by the observation of yeast growth on media lacking histidine or histidine/adenine. Yeast transformation and screening methods were described in the Yeast Protocols Handbook and the manufacturer's instructions (Clontech).

Restrained Docking Calculations. Two docking methods, HADDOCK (7) and surFit (http://sysimm.ifrec.osaka-u.ac.jp/surFit/), were used to generate representative TICAM-2 TIR homo-dimer models, from which trimeric TICAM-2/TICAM-1 models were then constructed. By ranking the resulting trimeric models by their consistency with the mutagenesis experiments, unfeasible TICAM-2 homodimer models were eliminated. TICAM-1 was then redocked at higher resolution to each of the surviving TICAM-2 homo-dimer models. Final selection was made by carrying out binding energy calculations using the EMPIRE (8) scoring function in combination with structural refinement of the wild-type and mutant forms of the top-scoring trimeric models.

Immunoprecipitation and Immunoblot Analysis. HA-tagged TICAM-1(1–566)-RHIM-mutant (V687A/Q688A/L689A/G690A) and FLAG-tagged TICAM-2(1–235) mutants were subcloned into pEF-BOS vector (9). TLR4 and MD2 expression plasmids were constructed as in a previous report (1). TICAM-1 and TICAM-2 mutants were transfected into HEK293FT cells using Fugene HD. Twenty-four hours after transfection, cells were harvested and lysed by 50 mM Tris·HCl (pH 7.5)-150 mM NaCl-1.0% Nonidet P-40-5 mM Na3VO4-30 mM NaF-X1 Protease inhibitor (Roche). FLAG-tagged TICAM-2 were immunoprecipitated using anti-FLAG mAb (2.5 μg per sample) and Protein G Sepharose (GE healthcare). Total lysates and immunoprecipitated proteins were analyzed by SDS/PAGE and immunoblotting using anti-FLAG pAb (Sigma) and anti-HA mAb (Roche) for the detection of TICAM-2 and TICAM-1.

Luciferase Reporter Gene Assay. Mutants of TICAM-1(1–566) and TICAM-2(1–235) were generated using PCR and subcloned into pEF-BOS vector. HEK293FT cells (Invitrogen) were maintained in Dulbecco's Modified Eagle's medium high glucose supplemented with MEM NEAA (Gibco), 10% heat-inactivated FCS, and antibiotics. Cells were transfected with TICAM-1 and TICAM-2 expression plasmids, IFN-β promoter plasmid, and an internal control plasmid coding *Renilla* luciferase using Fugene HD (Promega). Twenty-four hours after transfection, cells were lysed with Reporter Lysis Buffer (Promega). Luciferase activity was measured using Dual-Glo Luciferase Assay System (Promega). The *Firefly* luciferase activity was normalized to the *Renilla* activity and expressed as the fold-stimulation relative to the activity of vector-transfected cells. All assays were performed in triplicate.

1. Tao X, Xu Y, Zheng Y, Beg AA, Tong L (2002) An extensively associated dimer in the structure of the C713S mutant of the TIR domain of human TLR2. *Biochem Biophys Res Commun* 299(2):216–221.
2. Delaglio F, et al. (1995) NMRPipe: A multidimensional spectral processing system based on UNIX pipes. *J Biomol NMR* 6(3):277–293.
3. Goddard TD, Kneller DG (2004) SPARKY 3 (University of California, San Francisco).
4. Güntert P (2004) Automated NMR structure calculation with CYANA. *Methods Mol Biol* 278:353–378.
5. Cornilescu G, Delaglio F, Bax A (1999) Protein backbone angle restraints from searching a database for chemical shift and sequence homology. *J Biomol NMR* 13(3):289–302.
6. Landt O, Grunert HP, Hahn U (1990) A general method for rapid site-directed mutagenesis using the polymerase chain reaction. *Gene* 96(1):125–128.
7. de Vries SJ, van Dijk M, Bonvin AM (2010) The HADDOCK web server for data-driven biomolecular docking. *Nat Protoc* 5(5):883–897.
8. Liang S, Zheng D, Zhang C, Standley DM (2011) Fast and accurate prediction of protein side-chain conformations. *Bioinformatics* 27(20):2913–2914.
9. Mizushima S, Nagata S (1990) pEF-BOS, a powerful mammalian expression vector. *Nucleic Acids Res* 18(17):5322.

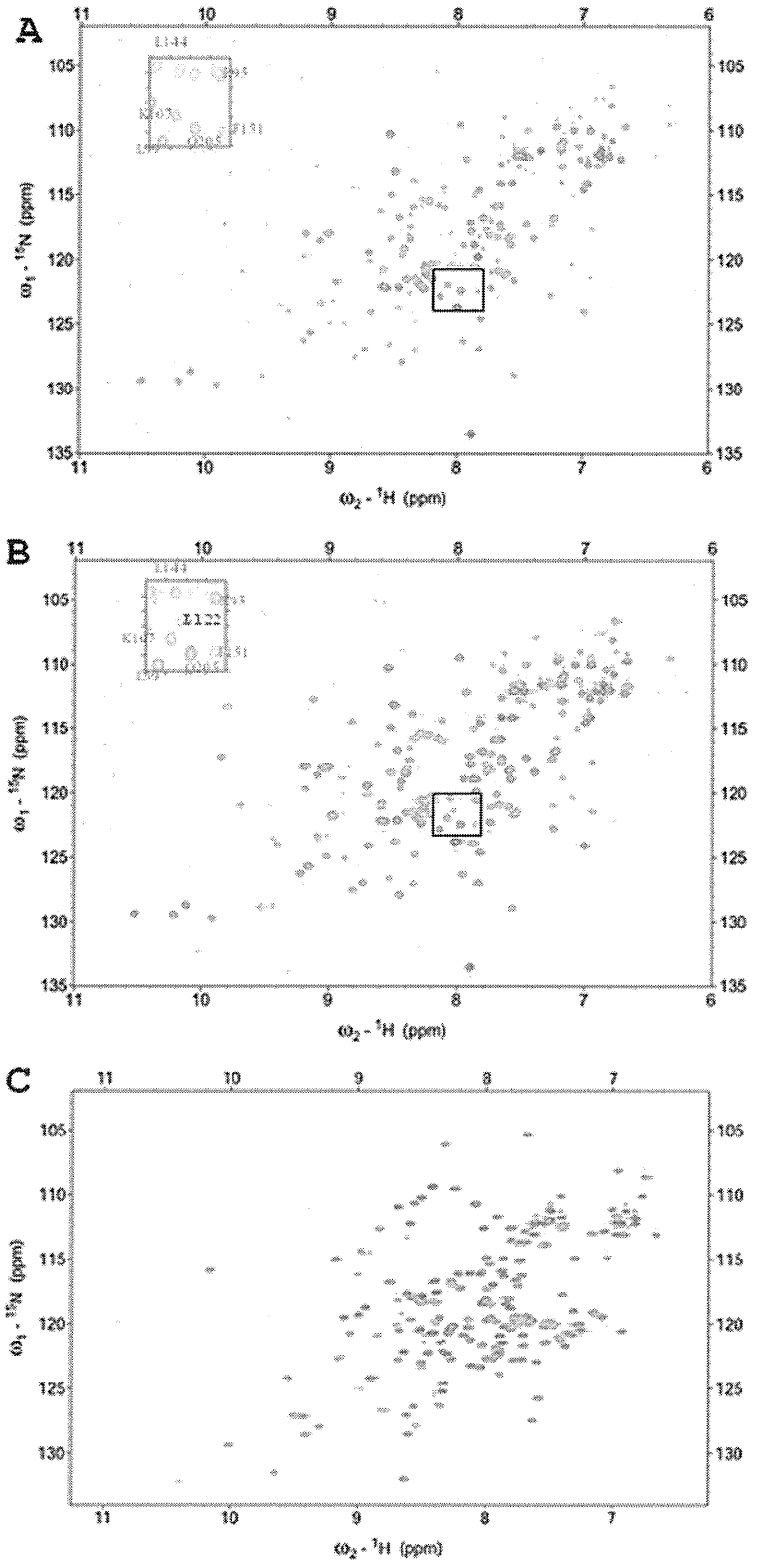

Fig. S1. [^{1}H,^{15}N]-HSQC spectra of the TIR domains of TICAM-1 and TICAM-2. (*A* and *B*) Comparison of HSQC spectra of the TICAM-2 wild type and C117H mutant under the same buffer conditions [50 μM ^{15}N-labeled proteins, 40 mM Hepes-NaOH (pH 7.2), 10 mM DTT, 10% glycerol, 90% H_2O/10% D_2O at 20 °C]. The *Inset* focused on Leu122 in the BB-loop in the wild type (*A*) and C117H mutant (*B*). (*C*) HSQC spectra of TICAM-1 P434H under acidic buffer conditions [0.3 mM ^{15}N-labeled protein, 20 mM AcOH buffer (pH 5.0), 10 mM DTT, 0.1 mM EDTA, 90% H_2O/10% D_2O at 20 °C].

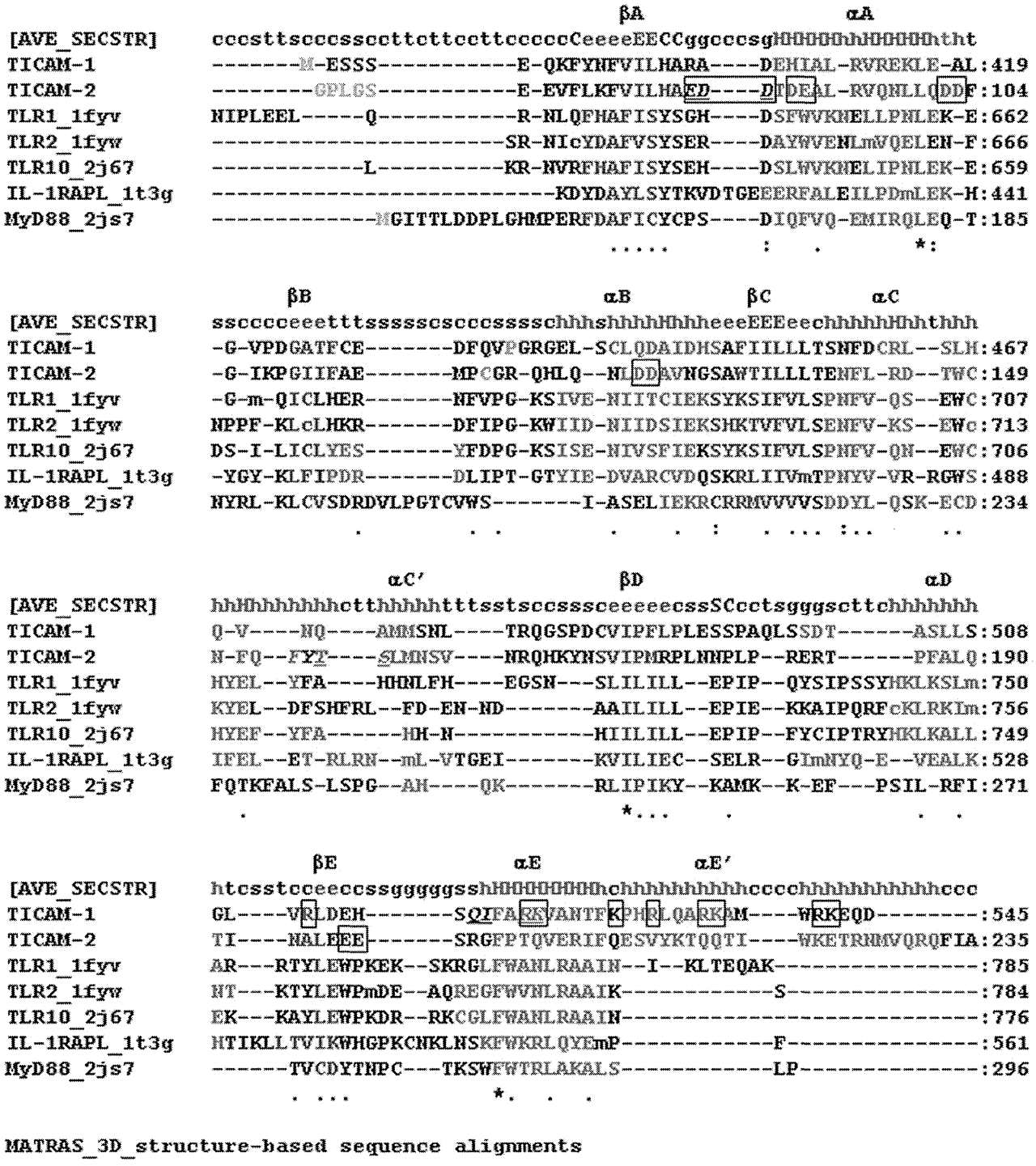

Fig. S2. Structure-based sequence alignments of TIR-domains. Structure-based sequence alignments were generated by the MATRAS web server. The average secondary structural elements of the TICAM-1 TIR are labeled on the top. α-Helices and β-strands are shown in red and blue, respectively. The boxes indicate acidic residues specific to the TICAM-2 TIR domain and basic residues specific to TICAM-1 TIR domain. Italics show interaction sites.

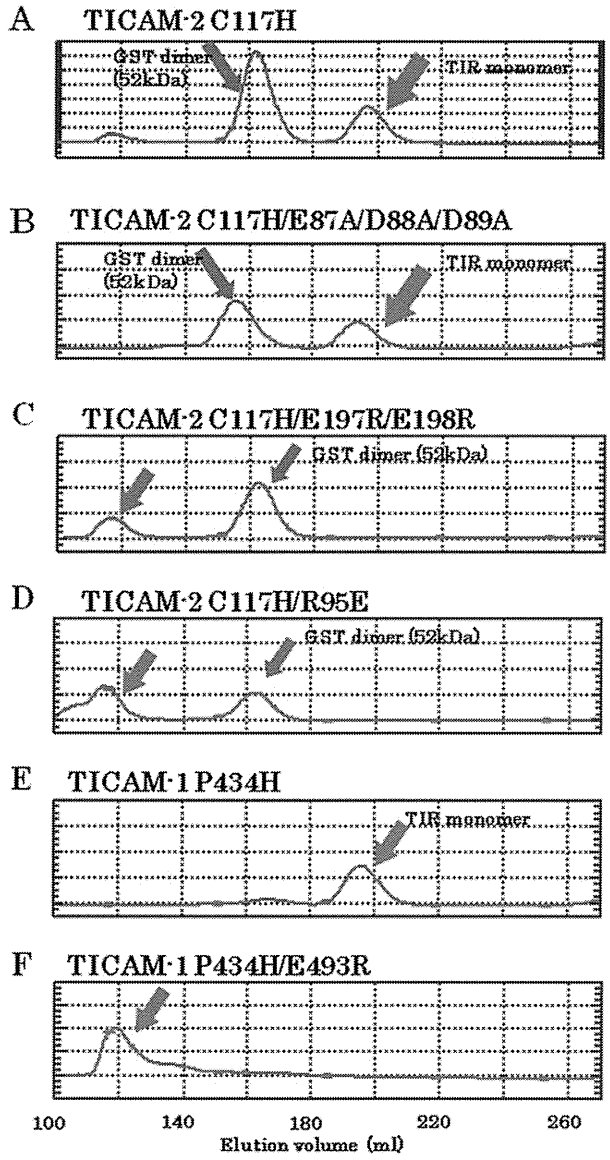

Fig. S3. Gel-filtration analysis of TIR domain mutants of TICAM-1 and TICAM-2. (*A*) TICAM-2 C117H, (*B*) TICAM-2 C117H/E87A/D88A/D89A, (*C*) TICAM-2 C117H/E197R/E198R, (*D*) TICAM-2 C117H/R95E, (*E*) TICAM-1 P434H, and (*F*) TICAM-1 P434H/E493R. The TIR monomer in *A*, *B*, and *E* indicates that elution volume is compatible with monomer size (~18 kDa). In *C*, *D*, and *F*, gel-filtration chromatography peaks appeared in the void position due to formation of high-molecular weight soluble aggregates.

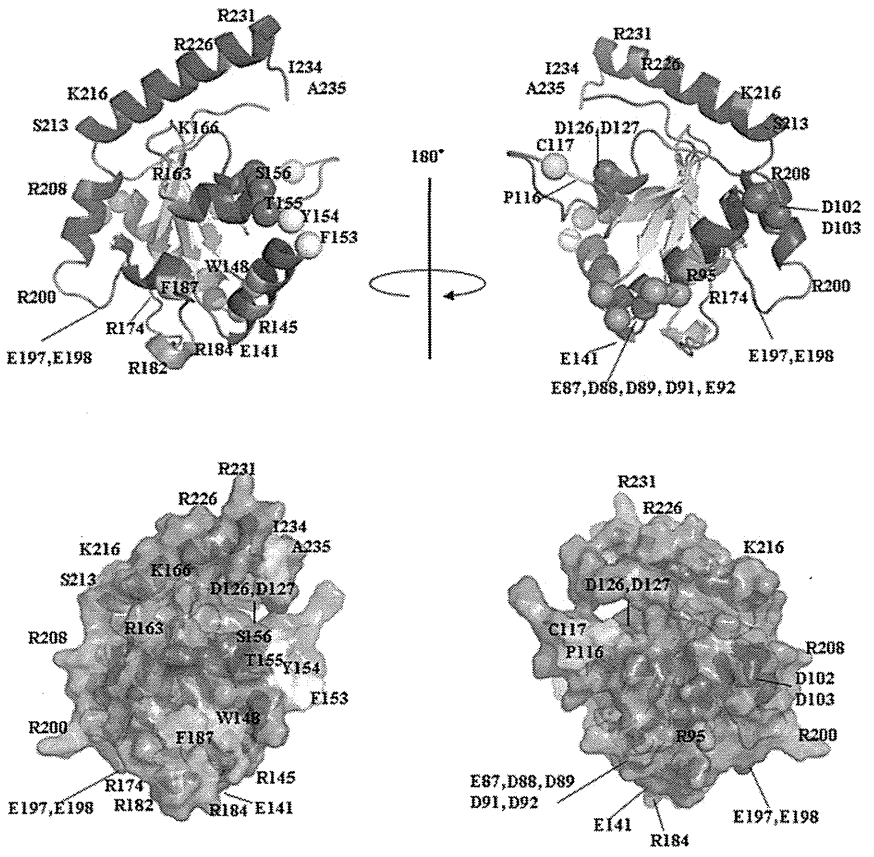

Fig. S4. Summary of mutations of TICMA-2 TIR applied to yeast two-hybrid assays. All mutations applied to yeast two-hybrid assays were mapped on the TIR domain of TICAM-2 C117H. Selected mutations are located on the exposed surface of the α-helices and the loop regions. Acidic residues are shown in orange and magenta. Basic residues are shown in green. Hydrophobic residues are shown in yellow-green. Pro116 and Cys117 are shown in yellow. Thr155 and Ser156 are shown in blue. Phe153 and Tyr154 are shown in white.

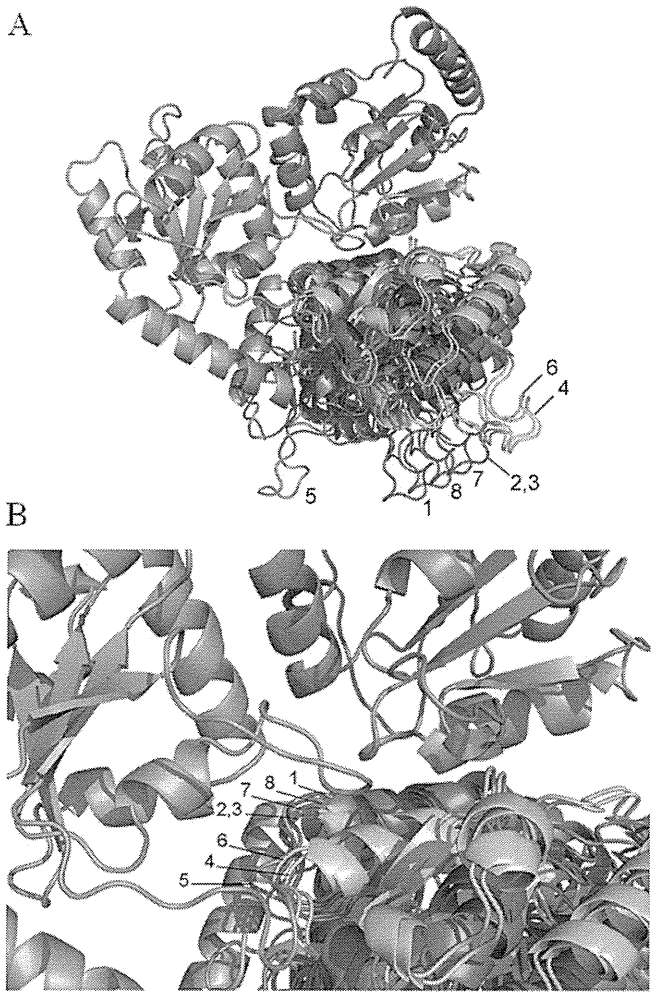

Fig. S5. Ensemble of top-ranked trimer models. (*A*) A global view of the top eight models is shown. (*B*) A close-up view of the top-ranked models at the TICAM-1/TICAM-2 interface is shown.

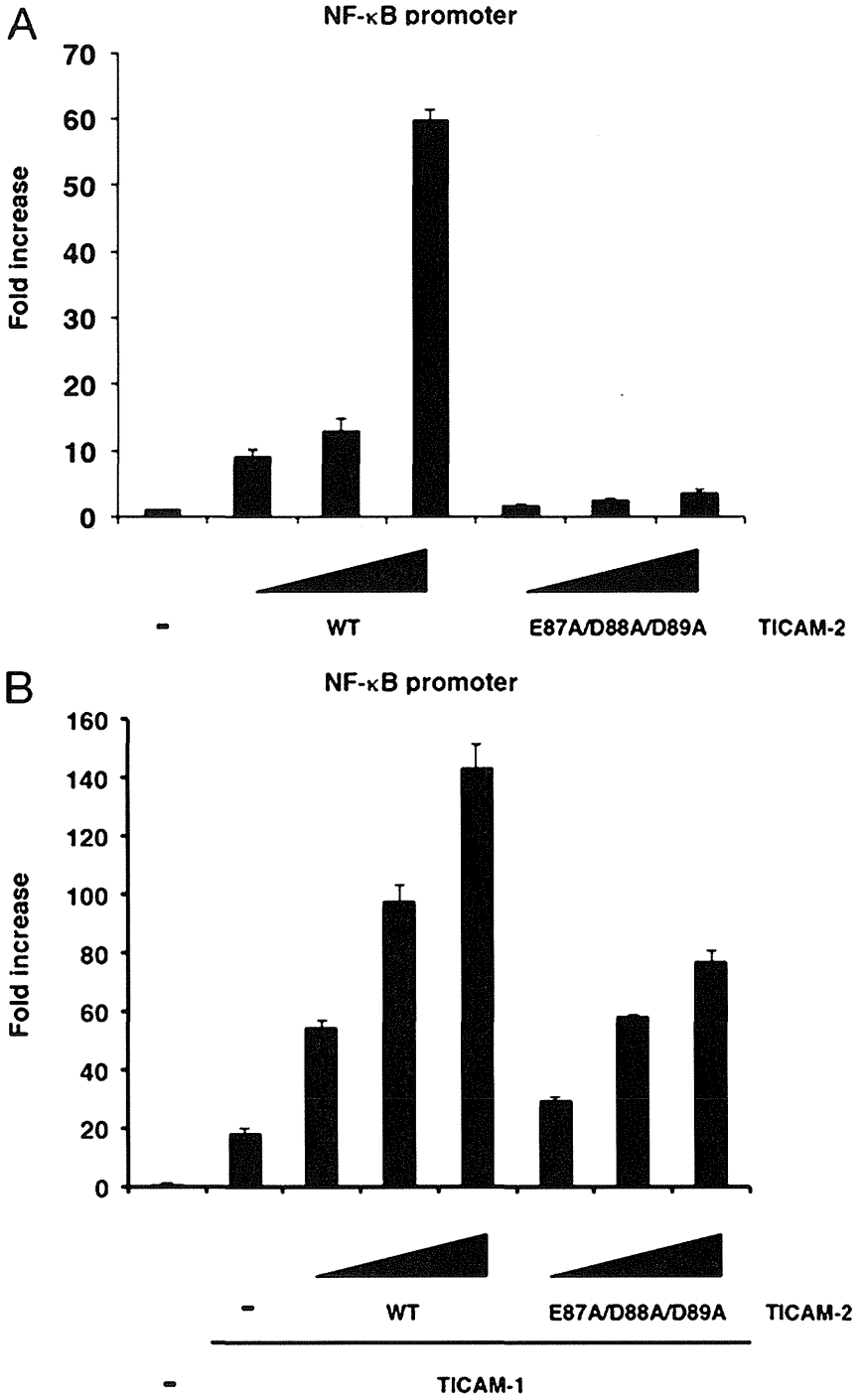

Fig. S6. Reporter assays of NF-κB activation. (*A*) HEK293FT cells preseeded onto 96-well plates were transfected with empty vector or increasing amounts of expression vector for wild-type or mutant TICAM-2 (10, 20, 70 ng per well) together with NF-κB reporter plasmid (25 ng per well) and internal control plasmid (5 ng per well). The total amount of DNA was kept at 100 ng per well by adding empty plasmid. Luciferase activity was measured 24 h after transfection. (*B*) TICAM-2-TICAM-1–dependent NF-κB activation. Cells were transfected with empty vector or indicated TICAM-2 expression plasmids (10, 20, 70 ng per well) together with a limiting amount of TICAM-1 expression plasmid (0.1 ng per well), NF-κB reporter plasmid (25 ng per well), and internal control plasmid (5 ng per well). Representative data from a minimum of three separate experiments are shown.

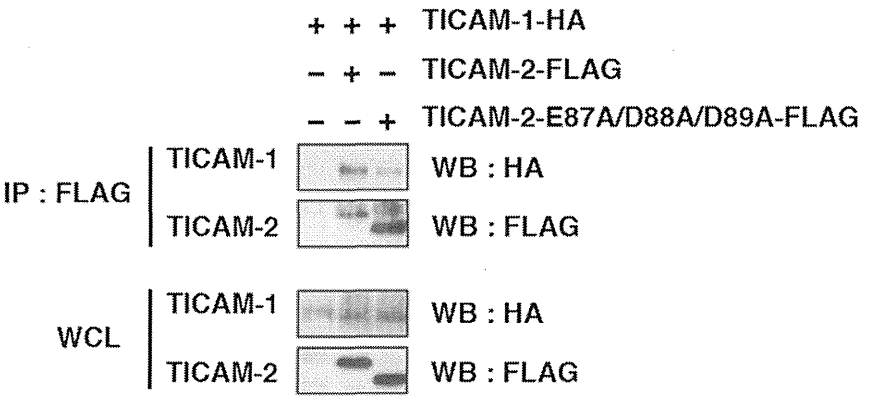

Fig. S7. Immunoprecipitation and immunoblot analysis of TICAM-1 and TICAM-2 interaction.

Table S1. Structural statistics for the 20 structures of lowest energy

	TICAM-1	TICAM-2
NOE distance restraints		
All	3,254	2,699
Sequential ($\|i - j\| = 1$)	1,954	1,481
Medium range ($2 \leq \|i - j\| \leq 4$)	640	529
Long range ($\|i - j\| > 4$)	660	689
Dihedral angle restraints (derived from TALOS)		
φ	104	128
ψ	104	135
Violations		
Distance > 0.5 Å	0	0
Angle > 5°	0	0
rmsd from the mean coordinates (secondary structures)*		
Backbone heavy atoms, Å	0.45	0.50
All heavy atoms, Å	0.84	1.01
Ramachandran plot statics, %†		
Residues in most favorable regions, %	71.6	77.7
Residues in additional allowed regions, %	27.7	22.0
Residues in generously allowed regions, %	0.7	0.3
Residues in disallowed regions, %	0.0	0.0

*The rmsd were calculated for the core region (395–427,442–527) of TICAM-1, and region (83–110,150–215) of TICAM-2.
†Values were calculated with PROCHEK.

Table S2. Summary of results of yeast two-hybrid analyses for mutation of TICAM-1

		Interaction (yeast growth)	
Number of amino acid	Secondary structure	Homotypic	Heterotypic
TICAM-1 (E387-D545)		TICAM-1	TICAM-2
P434H	BB-loop	−	+
R512A	DD-loop	+	+
R522A	αE-helix	+	−
K523A	αE-helix	+	−
R522A/K523	αE-helix	+	−
K529A	αE-helix	+	+
K529A/R532A	αE,αE′-helix	+	+
R532A	αE′-helix	+	+
R541A/K542A	αE′-helix	+	+
P434H/R512A		−	+
P434H/R522A/K523A		−	−
P434H/K529A		−	+
P434H/R532A		−	+
D484A	CD-loop	+	+
E493A	DD-loop	−	−
P434H/D484A		−	+
S495R/A497R	DD-loop	+	+
S495R/A497R/Q498R		+	+
E493R/S495R/A497E/Q498R	DD-loop	−	−
P496G	DD-loop	+	+

+, indicates that yeast can grow on SD-LWHA medium; −, indicates that yeast cannot grow on SD-LWHA medium. Empty cells indicate no data.

Table S3. Summary of results of yeast two-hybrid analyses for mutation of TICAM-2

		Interaction (yeast growth)	
Number of amino acid	Secondary structure	Homotypic	Heterotypic
TICAM-2 (E75-A235)		TICAM-2	TICAM-1
P116H	BB-loop	−	−
C117H	BB-loop	−	−
E87A/D88A/D89A	AA-loop		−
D91A/E92A	αA-helix		+
D102A/D103A	AB-loop		+
D126A/D127A	αB-helix		+
E197A/E198A	EE-loop		−
S64-A235	Extension of N terminus	+	+
E70-A235	Extension of N terminus	+	+
R95A	αA-helix	−	−
E141R	CC-loop	+	+
R231E	C terminus	+	+
R95A/R231E		−	−
E141R/R231E		+	+
R95A/E141R/R231E		−	−
E75-S213*	deletion of C terminus	−	−
E75-R226*	deletion of C terminus	+	+
I234E/A235D	C terminus	+	+
R231E/I234E/A235D	C terminus	+	+
C117H/E114R	BB-loop	−	
C117H/R119E	BB-loop	−	
C117H/E114R/R119E	BB-loop	−	

+, indicates that yeast can grow on SD-LWHA medium; −, indicates that yeast cannot grow on SD-LWHA medium. Empty cells indicate no data.

Table S4. *In silico* binding energy calculations for trimeric models ranked 1–5

Type of amino acid	Rank 1	2	3	4	5
TICAM-1 (E387-D545)					
P434H	+	+	+	+	+
R512A	+	+	+	–	+
R522A	–	–	–	–	–
K523A	–	–	–	–	–
R522A/K523	–	–	–	–	–
K529A	+	+	+	+	+
K529A/R532A	+	+	+	+	+
R532A	+	+	+	+	+
R541A/K542A	+	+	+	+	+
P434H/R512A	+	+	+	+	+
P434H/R522A/K523A	–	–	–	–	–
P434H/K529A	+	+	+	+	+
P434H/R532A	+	+	+	+	+
D484A	+	+	+	+	+
E493A	+	+	+	–	+
P434H/D484A	+	+	+	+	+
S495R/A497R	+	+	+	+	+
S495R/A497R/Q498R	+	+	+	+	+
E493R/S495R/A497E/Q498R	+	+	+	+	+
P496G	+	+	+	+	+
P434H/Q518A/I519A	–	–	–	–	–
TICAM-2 E75-A235)					
P116H	+	+	+	+	+
C117H	+	+	+	–	+
E87A/D88A/D89A	–	–	–	–	–
D91A/E92A	–	–	+	+	–
D102A/D103A	+	+	+	+	+
D126A/D127A	+	+	+	+	+
E197A/E198A	+	–	–	+	+
R95A	+	+	+	+	+
E141R	+	+	+	–	+
R231E	+	+	+	+	+
R95A/R231E	+	+	+	+	+
E141R/R231E	+	+	+	–	+
R95A/E141R/R231E	+	+	+	+	+
I234E/A235D	+	+	+	+	+
R231E/I234E/A235D	+	+	+	+	+
F153A/Y154S	+	–	–	–	+
T155A/S156A	–	–	–	–	–

A gray background indicates disagreement between calculation and experiment.

Biochemical and Biophysical Research Communications 437 (2013) 127–133

Contents lists available at SciVerse ScienceDirect

Biochemical and Biophysical Research Communications

journal homepage: www.elsevier.com/locate/ybbrc

Valine, the branched-chain amino acid, suppresses hepatitis C virus RNA replication but promotes infectious particle formation

Hisashi Ishida [a], Takanobu Kato [b], Kenji Takehana [c], Tomohide Tatsumi [a], Atsushi Hosui [a], Takatoshi Nawa [a], Takahiro Kodama [a], Satoshi Shimizu [a], Hayato Hikita [a], Naoki Hiramatsu [a], Tatsuya Kanto [a], Norio Hayashi [d], Tetsuo Takehara [a,*]

[a] Department of Gastroenterology and Hepatology, Osaka University Graduate School of Medicine, 2-2, Yamadaoka, Suita, Osaka, Japan
[b] Department of Virology II, National Institute of Infectious Diseases, Tokyo, Japan
[c] Exploratory Research Laboratories, Research Center, Ajinomoto Pharmaceuticals, Co, Ltd., Kanagawa, Japan
[d] Kansai Rosai Hospital, Amagasaki, Hyogo, Japan

ARTICLE INFO

Article history:
Received 3 June 2013
Available online 24 June 2013

Keywords:
Hepatitis C virus
Branched-chain amino acid
IRES activity
Infectious virus production
Mammalian target of rapamycin
JAK/STAT pathway

ABSTRACT

Background & aims: Concentrations of the branched-chain amino acid (BCAA) in the serum of patients with liver cirrhosis correlate with their liver function. Oral administration of BCAA can ameliorate hypoalbuminemia and hepatic encephalopathy. In this study, we aim to clarify the role of BCAA in regulating the replication of the hepatitis C virus (HCV).
Methods: HCV sub-genomic replicon cells, genome-length replicon cells, and cells infected with cell culture-infectious HCV (HCVcc) were cultured in media supplemented with various concentrations of BCAA, followed by evaluation of the replicon or HCV abundance.
Results: BCAA was capable of suppressing the HCV replicon in a dose-dependent manner and the effect was independent of the mTOR pathway. Of the three BCAAs, valine was identified as being responsible for suppressing the HCV replicon. Surprisingly, an abundance of HJ3-5(YH/QL), an HCVcc, in Huh7 cells was augmented by BCAA supplementation. In contrast, BCAA suppressed an abundance of HJ3-5(wild), an HCVcc that cannot assemble virus particle in Huh7 cells. Internal ribosome entry site of HCV was shown to be a target of BCAA. Single-cycle virus production assays using Huh7-25 cells, which lacked CD81 expression, revealed that BCAA, especially valine, promoted infectious virus particle formation with minimal effect on virus secretion. Thus, BCAA was found to have two opposing effects on HCV production: suppression of the HCV genome RNA replication and promotion of infectious virus formation.
Conclusions: BCAA accelerates HCV production through promotion of infectious virus formation in infected cells despite its suppressive effect on HCV genome replication.

1. Introduction

Persistent infection of hepatitis C virus (HCV) causes progressive liver disease in humans. Chronic inflammation in the liver leads to the accumulation of fibrosis and an eventual progression to liver cirrhosis. In patients with decompensated liver cirrhosis, a change in plasma amino acid composition is frequently observed. In particular, the ratio of branched-chain amino acid (BCAA) to aromatic amino acid (AAA), known as Fischer's ratio, decreases as the liver function deteriorates [1]. In such cirrhotic patients, hypoalbuminemia occurs, and it has been shown that oral administration of BCAA can ameliorate hypoalbuminemia and hepatic encephalopathy.

Three amino acids valine, leucine, and isoleucine are BCAAs, which are considered to be essential for protein anabolism. In addition to the role of acting as nutrient substrates, recent studies have demonstrated that BCAA also serve as physiologically active substances. BCAA have been shown to have pharmacological effects, such as induction of protein synthesis [2] and glucose metabolism [3]. In rat primary hepatocytes, albumin synthesis is significantly increased by BCAA administration, which is dependent on activation of the mammalian target of rapamycin (mTOR), mainly induced by leucine [4].

HCV replication is controlled by intracellular signaling pathways. In addition to the interferon (IFN)-induced JAK/STAT pathway, which activates interferon-stimulated genes, leading to strong anti-viral activity, activation of ERK [5], PI3 kinase/Akt [6,7], smad [8], PKC [9], and p38 [10], have been shown to be capable of regulating HCV replication. mTOR, one of the downstream molecules of Akt, phosphorylates the two substrates p70 S6 kinase and eukaryotic translation initiation factor 4E binding protein 1

* Corresponding author. Address: Department of Gastroenterology and Hepatology, Osaka University Graduate School of Medicine, 2-2, Yamadaoka, Suita, Osaka 565-0871, Japan. Fax: +81 6 6879 3629.
E-mail address: takehara@gh.med.osaka-u.ac.jp (T. Takehara).

0006-291X/$ - see front matter © 2013 Elsevier Inc. All rights reserved.
http://dx.doi.org/10.1016/j.bbrc.2013.06.051

(4EBP1). p70 S6 kinase phosphorylates ribosomal S6 protein, resulting in an increase of the protein synthesis complex. Phosphorylated 4EBP1 results in its dissociation from the eukaryotic translation initiation factor 4E (eIF4E), which consequently enables eIF4E to regulate the translation initiation. Thus, together, p70 S6 kinase and 4EBP1 are responsible for the mTOR-dependent regulation of cellular translation. Moreover, both have been demonstrated to be involved in the regulation of HCV replication [6].

The finding that BCAA, per se, can activate signaling pathways suggests that they may affect HCV replication, presumably via the activation of the mTOR pathway. However, to date, no detailed investigation has been reported. Therefore, we attempt to clarify whether BCAA have a role in regulating HCV replication by using the HCV replicon system and cell culture of infectious-HCV (HCVcc). The present study reveals that although BCAA, especially valine, suppresses HCV genome replication, they eventually promote total HCV production by accelerating viral formation.

2. Methods

2.1. Cells

The hepatoma-derived cell line Huh7 and its derivatives, Huh7.5 and Huh7-25 [11], were maintained in DMEM supplemented with 10% FCS. The HCV subgenomic replicon cell line Huh-RepSI [10], and the HCV genome-length replicon cell line 2–3 [12], both harboring the HCV-N strain (genotype 1b), were previously described. The molar ratio of the BCAA mixture was adjusted to Leu:Ile:Val = 2.0:1.0:1.2 according to data from previous studies [13]. For assays to examine the role of BCAA, cells were cultured in BCAA-deficient DMEM with 10% FCS supplemented with BCAA mixtures of various concentrations (0–2 mM).

2.2. Cell culture-infectious HCV

JFH-1 is a cell culture-infectious virus of genotype 2a as previously described [14]. HJ3-5(YH/QL) is a chimeric cell culture-infectious virus with a genome consisting of the core to NS2 sequence of genotype 1a (H77) virus placed within the background of the genotype 2a JFH-1 virus. This virus contained compensatory mutations in E1 (Y361H) and NS3 (Q1251L) [15]. These two mutations rendered the chimeric RNA highly infectious.

2.3. In Vitro transcription and transfection of synthetic RNA

Plasmid DNAs encoding HJ3-5(wild) and HJ3-5(YH/QL), a wild-type chimeric virus and a chimeric virus carrying two mutations, respectively, were linearized by *XbaI* prior to transcription. RNA was synthesized with the T7 RiboMAX Express Large Scale RNA Production System (Promega, Madison, WI, USA) following the

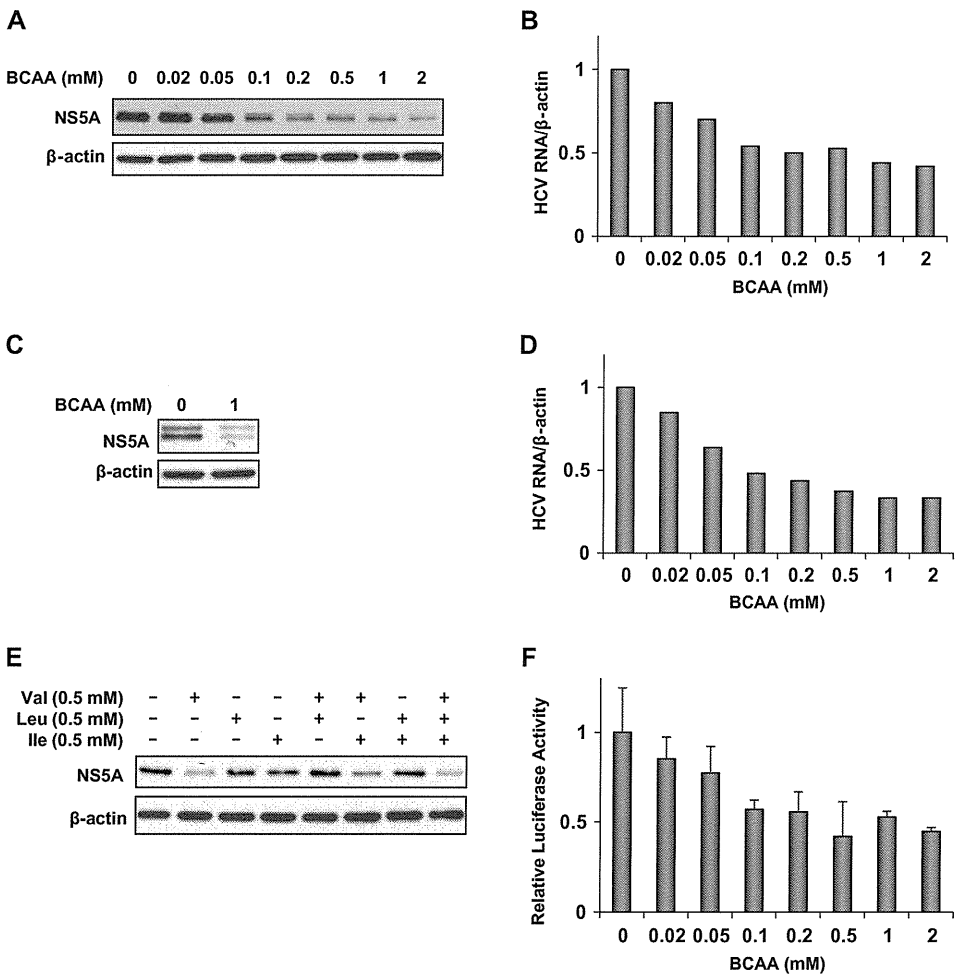

Fig. 1. BCAA limits the abundance of HCV replicon in HCV replicon cells. (A–D). Huh-RepSI (A and B) and 2–3 (C and D) cells were cultured in media for 2 days, with BCAA supplemented at concentrations of 0–2 mM. Total protein or total RNA was recovered and assayed for immunoblot (A and C) or real-time RT-PCR (B and D), respectively. (E) Three BCAAs (0.5 mM each) were added to BCAA-free culture medium of Huh-RepSI. After incubation for 2 days, immunoblot analysis of NS5A and beta-actin were performed. (F) Huh-RepSI cells were transfected with pRLHL, cultured in media with various BCAA concentrations between 0 and 2 mM. After incubation for 2 days, a dual luciferase assay was performed. The ratio of firefly luciferase activity to renilla luciferase activity was then calculated.

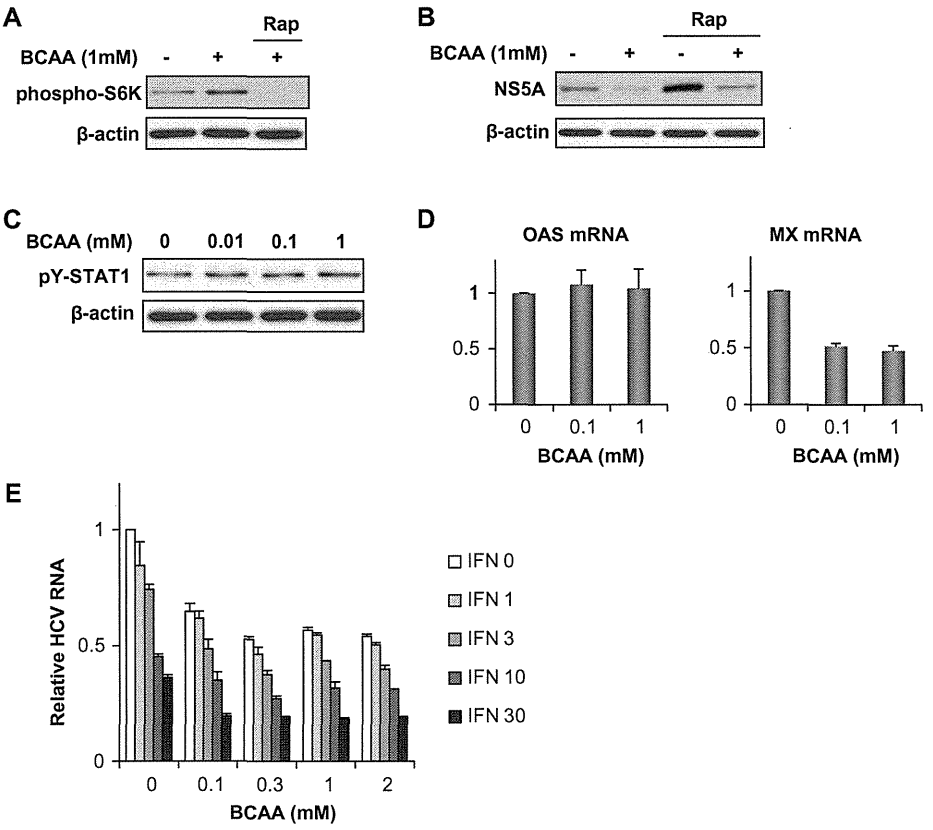

Fig. 2. BCAA-induced suppression of HCV replicon is independent of mTOR or JAK/STAT signaling. (A) Immunoblot of phosphorylated p70 S6 kinase and beta-actin in Huh-RepSI cells cultured in a medium with or without BCAA (1 mM). Rapamycin was added at 100 nM to the BCAA-containing medium. (B) Immunoblot analysis of NS5A and beta-actin in Huh-RepSI cells cultured in a medium with 1 mM BCAA or rapamycin (100 nM). (C) Huh-RepSI cells were incubated in media with various BCAA concentrations (0, 0.01, 0.1, 1 mM), and then, immunoblot analyses of phosphorylated STAT1 (Tyr701) and beta-actin were performed. (D) Huh-RepSI cells were incubated in media with various BCAA concentrations (0, 0.1, 1 mM), and then, a real-time RT-PCR analysis, for expression of OAS and MX, was performed. (E) Huh-RepSI cells were incubated in culture media with various BCAA concentrations (0–2 mM) and IFN-α (0–30 U/ml). HCV RNA abundance was normalized with beta-actin allowing the relative HCV RNA levels to be calculated, setting the HCV RNA level of 0 U/ml IFN-α and 0 mM BCAA as 1. Rap: rapamycin.

manufacturer's suggested protocol. For electroporation, Huh7 cells were washed twice with ice cold phosphate-buffered saline (PBS) and resuspended at a concentration of 10^7 cells/ml in PBS. Subsequently, 10 μg of RNA was mixed with 500 μl of the cell suspension in a cuvette, with a gap width of 0.2 cm (GenePulser II System; Bio-Rad, Hercules, CA, USA). The mixture was immediately subjected to two pulses of current with the intensities of 1.2 kV, 25 μF, and maximum resistance. Following a 10-min incubation at room temperature, the cells were transferred into growth medium.

2.4. Titration of HCV infectivity

Huh-7.5.1 cells were seeded in 96-well plates at a density of 1×10^4 cells per well 24 h prior to culture media inoculation of the HCV infected cells. Three days after infection, HCV-positive cells were detected with mouse monoclonal antibody that recognized core proteins stained with an Alexa Fluor 488 anti-mouse secondary antibody (Invitrogen, Carlsbad, CA, USA). The infectivity titer was expressed as focus-forming units per mL of supernatant (ffu/mL), expressing the mean number of HCV core-positive foci. The intracellular infectivity and specific intracellular infectivity titer were determined as described previously [16].

3. Results

3.1. BCAA suppresses the amount of HCV replicon

To investigate the role of BCAA in HCV replication, we first examined the effect of BCAA on the HCV replicon. An HCV subgenomic replicon cell line, Huh-RepSI, was incubated in culture medium that contained various concentrations of BCAA (0–2 mM) for 2 days. HCV replicon RNA, as well as the amount of protein, was suppressed by adding BCAA in a dose-dependent manner (Fig. 1A and B). To confirm the effect of BCAA, another replicon cell line, 2–3, carrying a genome-length HCV replicon, was used. In this experiment, suppression of the replicon by BCAA was observed, which is in agreement with the Huh-RepSI assay (Fig. 1C and D). This activity suggested that BCAA possessed the ability to suppress HCV replication.

Three BCAAs exist: valine, leucine, and isoleucine. As previously demonstrated, leucine contains the biological activity to activate mTOR. In addition, we showed that mTOR, which is activated by PI3 kinase/Akt, was able to suppress HCV replication [6]. Therefore, it is possible that the BCAA-mediated suppression of HCV replication was due to leucine. To test this hypothesis, the three amino acids were added independently to BCAA-deficient medium while monitoring the HCV replication level. Unexpectedly, the result refuted the hypothesis (Fig. 1E). Compared to the cells cultured in BCAA-deficient medium, supplementation with only valine efficiently suppressed the HCV replicon, whereas leucine did not; instead, it caused a slight increase. This result showed that BCAA, especially valine, but not leucine, have a suppressive effect on HCV replication.

3.2. BCAA suppresses HCV IRES activity

HCV replication can be controlled by HCV specific translation regulated by IRES, the 5′ UTR region of HCV. Therefore, we next

investigated the effect of BCAA on HCV IRES activity. To do this, we utilized a dicistronic vector, pRLHL, which consists of firefly luciferase driven by HCV IRES and renilla luciferase, translated in a cap-dependent manner (Sup. Fig. 1). Relative HCV IRES activity was evaluated using the ratio of IRES-specific luciferase activity to the cap-dependent luciferase activity. As shown in Fig. 1F, HCV IRES activity was suppressed by BCAA in a dose-dependent manner, which is similar to the result of the replicon abundance (Fig. 1A and B). Thus, the BCAA-mediated suppression of HCV replication is likely due to the inhibition of HCV IRES activity.

3.3. BCAA-mediated suppression of HCV replicon is independent of the mTOR and JAK/STAT pathways

Previous reports have demonstrated that BCAA is capable of activating mTOR [4], and we have reported that mTOR suppresses HCV replication [6]. Therefore, we examined the contribution of mTOR activation on BCAA-mediated suppression of the HCV replicon. Administration of BCAA efficiently phosphorylated p70 S6 kinase, whereas rapamycin completely inhibited its phosphorylation (Fig. 2A). Despite rapamycin enhancing the amount of HCV replicon, BCAA could efficiently suppress it, even in rapamycin-containing medium (Fig. 2B), suggesting that the suppression of the HCV replicon by BCAA is independent of mTOR activation.

The IFN-JAK/STAT signal is known to be an anti-virus pathway, induced under the condition of virus infection. HCV replication is efficiently inhibited by interferon. Therefore, we examined whether BCAA could modify the IFN signal. First, we performed an immunoblot analysis and evaluated the status of STAT1 activation, in the presence or absence of BCAA. However, the phosphorylated STAT1 level was not altered by BCAA in Huh-RepSI cells, and ISG induction was not observed; instead, the expression level of Mx was suppressed by BCAA (Fig. 2C and D). A previous study showed that rapamycin diminished the suppressive effect of IFN-α toward HCV replication via the suppression of ISG induction [17]. Subsequently, we examined the HCV replicon abundance in cells that were cultured in media with various concentrations of BCAA and IFN-α stimuli. Even with the depletion of BCAA, IFN-α efficiently and dose-dependently suppressed HCV replicon abundance. However, IFN-α-induced anti-HCV activity was not augmented by BCAA supplementation (for example, the replicon RNA level decreased to approximately 30% in both BCAA-depleted medium and 2 mM BCAA-supplemented medium) (Fig. 2E). Consequently, BCAA did not influence JAK/STAT activation, and therefore, the suppression of HCV replicon by BCAA may have been independent of the IFN-α-induced signaling pathway.

3.4. BCAA enhances HCVcc production

Next, we examined the impact of BCAA on HCVcc, a system retaining the entire HCV life cycle in a cultured cell. Here, we used HJ3-5(YH/QL), a chimeric HCV of genotype 1a (H77) and 2a (JFH-1). Surprisingly, the results of HJ3-5(YH/QL) were opposite to that of the HCV replicon: HCV abundance was upregulated in a BCAA dose-dependent manner (Fig. 3A). The HCV replicon contains NS3 to NS5B proteins, which are required for HCV RNA genome replication, but not core, E1 and E2 proteins, which are structural proteins required for viral particle formation. The discrepancy in the results between HCV replicon cells and HCVcc-infected cells might be due to differences in virus particle production.

To investigate this discrepancy, we used the wild-type HJ3-5, designated as HJ3-5(wild). As described in the Methods section, HJ3-5(YH/QL) or the HCVcc used in this study, carries two amino acid substitutions at amino acid 361 and amino acid 1251, within E1 and NS3, respectively. These two mutations render the chimeric RNA highly infectious [15]. However, without these mutations, virus particle assembly and consequent virion release from the cells to the medium would not occur. This process is thought to be due to impaired association of the HCV proteins originating from different genotypes, whereas there is no apparent change in the HCV RNA replication level in the cells [15].

We introduced the *in vitro* transcribed genome RNA of HJ3-5(wild) or HJ3-5(YH/QL) into Huh7 cells with electroporation, and then, we examined the effect of BCAA on the cell line. Normally, synthesized HCV RNA introduced into cells executes replication by utilizing HCV proteins encoded in the genome and host factors, resulting in a robust increase that is detectable after 2–3 days. BCAA decreased the abundance of HJ3-5(wild), which was similar to their effect on the HCV replicon (Fig. 3B and C). Thus, HJ3-5(wild), a virus that is defective in virus particle formation, revealed the opposite reaction to BCAA compared to the virus HJ3-5(YH/QL), a virus that is competent in virus particle formation. Together, these findings revealed that although BCAA had the ability to suppress the HCV genome replication, they promoted viral production by enhancing other steps, which included virus assembly, virus particle release and cell re-infection.

3.5. BCAA promotes infectious HCV particle formation, not virus secretion

To further assess the BCAA intracellular mechanisms that influence the HCV life cycle, we adopted a single-cycle virus production assay [18]. We used Huh7-25 cells due to the lack of surface expression of one of the cellular HCV receptors, CD81, thus being non-permissive to HCV infection. Because HCV genome replication or virus production is intact in Huh7-25, we can evaluate viral replication and secretion without the influence of re-infection.

First, we studied the replication levels of the infectious virus, JFH-1, in Huh7-25 cells. The full length of the JFH-1 genome RNA

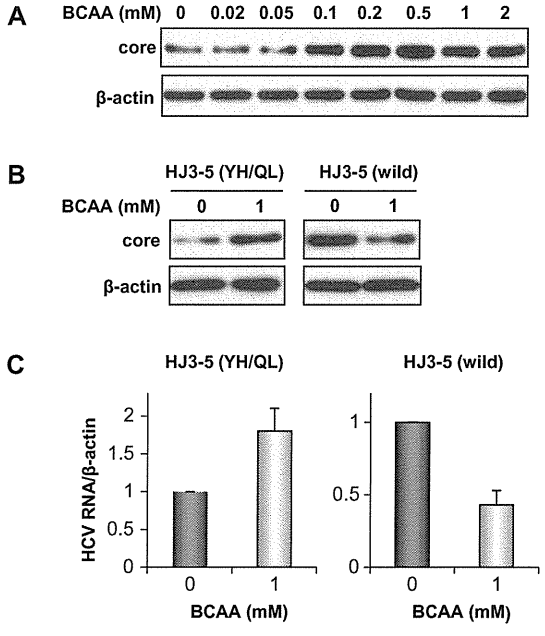

Fig. 3. HCVcc abundance was increased by BCAA. (A) HCVcc-infected Huh7 cells were cultured in media with various BCAA concentrations (0–2 mM). After incubation for 2 days, and an immunoblot analysis of core and beta-actin was performed. (B and C) Synthesized HCV genome RNA of HJ3-5 (YH/QL) or HJ3-5 (wild) was transfected into Huh7 cells via electroporation. After incubation for 24 h, cells were split into 6-well plates and incubated for 2 days in a culture medium with or without 1 mM BCAA. After the cells were harvested, immunoblot analysis of core and beta-actin (B) and real-time RT-PCR analysis (C) were performed.

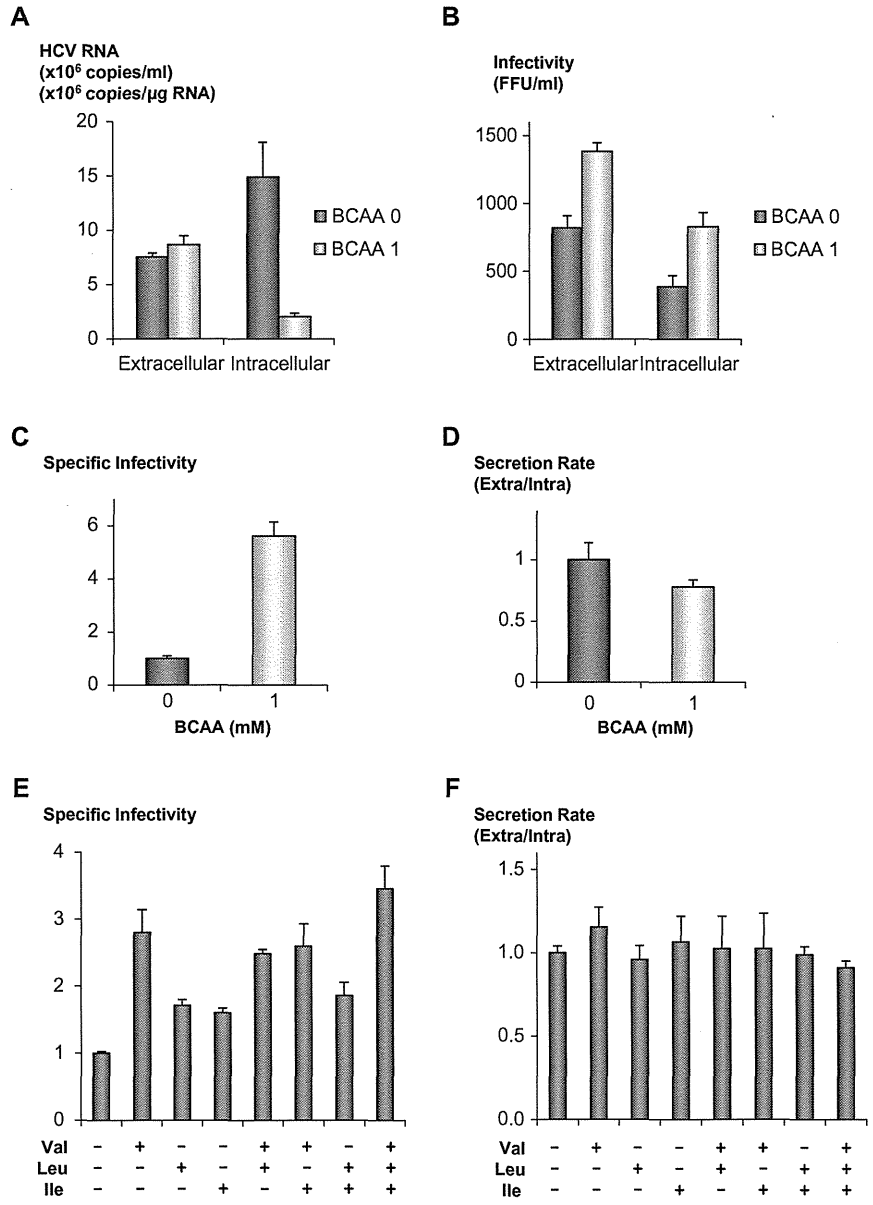

Fig. 4. Single-cycle virus production assay indicates a promoting effect of BCAA on virus formation. (A) Huh7-25 cells were transfected with *in vitro*-transcribed RNA of JFH-1, incubated in media with or without BCAA, followed by the RNA levels in the media or in the cells being calculated using the real-time quantitative RT-PCR method. (B) Infectivities in the media or in the cell lysates were measured. (C) Specific infectivities were calculated by dividing the infectivities by the HCV RNA amounts. (D) Secretion rates were calculated by dividing extracellular infectivities by intracellular infectivities. The data were presented as ratios defining the value of BCAA at 0 mM as 1. (E and F) Specific infectivities and secretion rates in the presence of valine (0.5 mM), leucine (0.5 mM), or isoleucine (0.5 mM). The data were presented as ratios defining the value with no BCAA as 1.

was translated *in vitro* and transfected into the Huh7-25 cells. The cells were cultured in media, with or without 1 mM of BCAA, with the RNA levels being monitored using quantitative RT-PCR. As observed in the experiment of replicon cells or virus particle formation-deficient viruses, the intracellular RNA level of HCV was suppressed by the presence of BCAA (Fig. 4A). However, the levels of extracellular HCV RNA were similar. Despite the suppression of intracellular HCV RNA levels by BCAA-containing medium, the infectivity titer of the intracellular virus in the cells treated with 1 mM BCAA was significantly higher than that of the cells with 0 mM BCAA (Fig. 4B). Extracellular infectivity titers were similar to those of intracellular infectivity. The specific infectivity of intracellular virus was calculated by dividing the infectivity titer by the HCV RNA level and this revealed that cultivation of the cells in a medium of 1 mM BCAA resulted in a 5.6-fold higher specific virus infectivity than that of 0 mM BCAA (Fig. 4C). Next, we measured virus secretion rates by dividing extracellular infectivity titers by intracellular infectivity titers. There was a minimal difference between infectious virus particle secretions (Fig. 4D). Thus, these results indicated that the infectious virion production was promoted in the BCAA-supplemented medium, although the virus RNA replication was suppressed.

In the study using replicon cells, valine was shown amino acid responsible for regulating HCV RNA replication (Fig. 1E). Finally, we assessed the effect of individual BCAA on virus production. HCV infected cells were cultured in media containing each amino acid at 0.5 mM or a combination of them and subsequently specific infectivity and secretion rate were examined (Fig. 4E and F). Among the three BCAAs, valine promoted infectious virus production most effectively, while leucine and isoleucine promoted infectious virus production modestly. Secretion rates did not show a significant difference.